https://doi.org/10.5194/egusphere-2026-6278
Preprint. Discussion started: 16 November 2026
© Author(s) 2026. CC BY 4.0 License.

Controls of shear scour and bend impact of glacial lake outburst floods: insights from the 2023 South Lhonak event

Pu Li[1], Kaiheng Hu[1], Li Wei[1], Hao Li[1]

[1]Key Laboratory of Mountain Hazards and Engineering Resilience/Institute of Mountain Hazards and Environment, Chinese Academy of Sciences, Chengdu, Sichuan 610213, China

Correspondence to: **Kaiheng Hu** (khhu@imde.ac.cn)

Abstract: Glacial lake outburst flood (GLOF) can entrain a massive amount of sediment from channel bed and banks as it travels downstream, and thereby amplifying its destructive potential. Yet most GLOF research has focused on bed erosion, whereas bank erosion has received far less attention. In this study, two mechanistically distinct modes of bank erosion, namely shear scour and bend impact, are investigated using pre- and post-event DEMs, high-resolution imagery, and HEC-RAS simulations of the South Lhonak Lake (SLL) outburst in Sikkim, India, on 3 October 2023, which caused severe damage to downstream infrastructure and settlements. Over the ~68-km-long study reach, the mean local maximum bank retreat rate at bend apex cross-sections was 4.28 cm/s during the effective erosion period (3700 s), higher than that of shear scour sites (2.51 cm/s). The mean effective erosion depth and post-event bank slope at bend impact sites were 52.7 m and 61.8°, respectively, compared with 15.2 m and 40.7° at adjacent shear-scour sites. Bend impact drives deep erosion through concentrated normal pressure, whereas shear scour removes material tangentially and produces a gentler slope. A mechanical model based on classical oblique jet theory shows that impact pressures at bend sites exceed bank shear stresses by about two orders of magnitude, confirming that normal impact pressure dominates bank failure at sharp concave banks. For shear-scour segments, normalized bank erosion rates form a funnel-shaped distribution as a function of the ratio between bank height and flow depth, with wide scatter at low ratios and narrowing at high ratios. This pattern reflects a transition from hydrodynamic control, in which local flow variability dominates, to bank-stability control, in which cantilever collapse limits retreat. Back-calculated apparent critical shear stresses from shear-scour segments vary considerably downstream, and all samples fall within the "very erodible" category, indicating that channel morphology controls the spatial concentration of flow energy. Together, these findings show that channel morphology determines whether bank erosion is dominated by shear scour or bend impact and modulates the apparent critical shear stress of bank material, providing a mechanistic basis for bank erosion calculation in GLOF-prone mountain valleys.

Keywords: Glacial lake outburst flood; Shear scour; Bend impact; Channel morphology; Effective erosion depth; Apparent critical shear stress

1. Introduction

Global warming is affecting High Asia unevenly, and over the past five decades the Tibetan Plateau and surrounding high mountains have warmed at about twice the global mean rate (Ballantyne et al., 2014; Intergovernmental Panel On Climate Change (Ipcc), 2023; Taylor et al., 2023; Yao et al., 2019; You et al., 2021; Zhang et al., 2023; Zheng et al., 2021). Widespread glacier retreat has followed, together

https://doi.org/10.5194/egusphere-2026-6278
Preprint. Discussion started: 16 November 2026
© Author(s) 2026. CC BY 4.0 License.

with sustained growth in the number and area of glacial lakes. Previous studies (Bolch et al., 2012; McColl and Davies, 2013; Nie et al., 2017; Shugar et al., 2020; Zhao et al., 2022a) reported that the number of glacial lakes in the Himalayan region increased by about 14.5 % over the past three decades, with total area expanding by about 18 %. Most of these lakes are impounded by loose, unstable moraine dams. Triggered by glacier calving, rock avalanches, or extreme rainfall, these dams can fail suddenly (Dunning et al., 2015; Furian et al., 2022; Taylor et al., 2023), rendering glacial lake outburst floods (GLOFs) that rank among the most destructive cryosphere hazards.

High Mountain Asia, particularly the Himalaya, has the highest GLOF susceptibility in the world (Komori et al., 2012; Wang et al., 2020; Zheng et al., 2021). Between 1833 and 2023, more than 700 GLOF events occurred in the Himalaya, and about 70 % of these occurred in the last 50 years (Miles et al., 2018; Shrestha et al., 2023). GLOF frequency has risen since 1980, with the average increasing from 1.5 events per year during 1981–1990 to 2.7 events per year during 2011–2020, and activity is particularly high in southeastern Tibet and along the China–Nepal border (Gouli et al., 2025). Several recent events illustrate the scale of the hazard. The 2016 Gongbatongshaco GLOF in Nepal traveled 40 km and destroyed a hydropower plant (Cook et al., 2018). On 8 July 2025, a glacial lake outburst flood in the Gyirong region of Tibet caused significant downstream damage (Zhang et al., 2026).

GLOFs differ from rainfall-generated river floods in ways that are directly relevant to bank erosion analysis (Jiang et al., 2026; Li et al., 2025). They originate in steep, high-elevation source areas where the elevation difference between the breach and the downstream terminus can exceed 3000 m, so that enormous potential energy converts into high flow velocities and extreme stream power per unit width (Allen et al., 2016; Klimeš et al., 2015). Rainfall floods typically diffuse downstream and their peak declines with distance, whereas GLOF peak discharge often remains high or even increases for tens of kilometers. This difference arises because the steep, confined valley prevents significant attenuation and because sediment entrainment and progressive bank collapse can amplify the flow. GLOFs also carry extremely high sediment concentrations and are strongly unsteady, with rapid rise and fall of stage (Gouli et al., 2025; Harrison et al., 2018). Because conventional river flood hydraulics does not capture these conditions, GLOF bank erosion cannot be reliably predicted by simply extrapolating theories developed for rainfall-generated river floods.

Bank erosion in GLOFs is more hazardous than channel widening alone. When powerful flows exert high shear stress along banks or impact the bank face directly, bank material is stripped layer by layer, the toe is progressively undercut, and the bank becomes increasingly steep and loses basal support (Cook et al., 2018; Kääb et al., 2021). Stress then redistributes within the slope, and failures can range from small collapses to large deep-seated landslides. These secondary landslides can destroy vegetation, roads, and buildings, and their deposits may block the main channel and form a dammed lake. If the dammed lake fails, the secondary flood peak can approach or even exceed the initial GLOF, creating a domino-like hazard chain of GLOF, bank erosion, landslide, dammed lake, and secondary breach (Cook et al., 2018; Cui et al., 2010; Mani et al., 2023; Sattar et al., 2022). In the 2021 Chamoli event (Shugar et al., 2021; Westoby et al., 2023), bank erosion and associated landslides played significant amplification roles. The Chamoli event showed that topographic constraints on flow dynamics can induce intense material

https://doi.org/10.5194/egusphere-2026-6278
Preprint. Discussion started: 16 November 2026
© Author(s) 2026. CC BY 4.0 License.

erosion and enhance mobility (Liu et al., 2026; Wang et al., 2024), which has important mechanistic parallels with GLOF bank erosion. Existing GLOF research has focused mainly on breach processes, flood routing and channel bed erosion, while the spatial patterns and mechanisms of fluvial bank erosion—specifically shear scour and bend impact—remain poorly studied. Gravitational landslides, although an important component of the GLOF hazard chain, are not treated as a separate bank erosion category in this study; they are identified and excluded so that the analysis can focus on the two types of fluvial bank erosion mechanisms.

The South Lhonak Lake (SLL) in Sikkim lies in the Upper Teesta Basin at 5200 m and is one of the largest, fastest-growing, and most hazardous lakes in Sikkim (Sattar et al., 2025). On 3 October 2023, SLL breached, and the resulting flood cascade killed 55 people and left 74 missing, destroying the 1200-MW Teesta-III hydropower dam. About 14.7 million m^3 of frozen moraine material slid into the lake, breaching the moraine dam and releasing about 50 million m^3 of water with a peak discharge of 48,500 m^3/s (Zhang et al., 2025). The flood eroded about 270 million m^3 in the approximately 68-km long reach downstream of the breach and triggered 44 landslides. A preliminary inspection of the pre- and post-event DEMs and high-resolution imagery revealed significant bank erosion along the study reach, especially on several sharp concave bends. This observation motivates the present analysis of bank shear scour and bend impact mechanisms in this reach.

To address these gaps, this study investigates bank erosion mechanisms at bend impact sites and along shear scour segments during the 2023 South Lhonak GLOF. Gravitational landslides are first identified and excluded using pre- and post-event DEMs and high-resolution imagery; they are not treated as a separate bank erosion category. The remaining bank erosion is then classified into bend impact and shear scour. A valley morphology index is introduced to characterize downstream changes in valley cross-sectional form. Two-dimensional hydraulic simulations provide peak flow parameters of the GLOF. A mechanical model based on classical oblique jet theory is applied to quantify bend impact erosion, and pre- and post-event DEMs together with Hydrologic Engineering Center–River Analysis System (HEC-RAS) simulation results are used to characterize the normalized bank erosion rate of shear scour segments. The analysis examines the spatial distribution of bank erosion, the relationship between channel morphology and bank erosion types, and the volumetric contribution of bend impact relative to shear scour, with the aim of improving hazard assessment for GLOFs in steep mountain regions.

2. Study area and data preparation

2.1 South Lhonak Lake and the 2023 GLOF Event

SLL (27° 56′ N, 88° 11′ E) is located in northwestern Sikkim, India, in the eastern Himalaya, at approximately 5200 m elevation (Aggarwal et al., 2017; Govindha Raj et al., 2013). The lake is a typical proglacial lake formed by continued retreat of the South Lhonak Glacier and impoundment by lateral and terminal moraines, with a lake area of about 0.5 km^2, fed mainly by glacier meltwater and upstream inflow. In recent decades, due to rapid regional warming, the South Lhonak Glacier has continued to thin and retreat, the lake basin has expanded, ice cores within the lateral moraine have degraded, permafrost creep has intensified, and bank stability has steadily declined (Sattar et al., 2021;

https://doi.org/10.5194/egusphere-2026-6278
Preprint. Discussion started: 16 November 2026
© Author(s) 2026. CC BY 4.0 License.

Singh et al., 2025). SLL is one of the largest, fastest-growing, and most dangerous lakes in Sikkim, with potential for major downstream destruction (Sattar et al., 2025). In the early morning of 3 October 2023, a large breach of the SLL moraine dam in Sikkim, India, initiated a devastating GLOF and caused severe damage to downstream infrastructure and settlements. About 14.7 million m^3 of frozen moraine material slid into the lake, breaching the moraine dam and releasing about 50 million m^3 of water with a peak discharge of 48,500 m^3/s. The outburst flood flowed down the Lhonak Chhu River, joined the Lachen River, and continued southward along the Teesta River, with a total impact distance of about 385 km, destroying the 1200-MW Teesta-III hydropower station (Fig. 1).

In the approximately 68-km-long main erosion reach below the breach (ending at the Teesta Stage-III dam), the flood strongly eroded the bed and banks, producing a total erosion volume of about 270 million m^3 and deposition of about 93 million m^3, with net erosion of about 177 million m^3. The valley transitions from an upstream glaciated U-shaped wide valley to a downstream fluvial narrow, deeply incised valley, with valley bottom width narrowing from hundreds of meters to tens of meters, and bed slope and bank height increasing significantly downstream. Correspondingly, flow energy shifts from dispersed to concentrated, and erosion types gradually shift from lateral widening to vertical incision and bedrock side-cutting. Within the study area, 44 secondary landslides were identified, 39 of which are distributed upstream of the Teesta Stage-III dam. Therefore, this study focuses on the 68-km main erosion reach from the lake breach to the Teesta Stage-III dam; Sattar et al. (2025) released pre-event (December 2018) and post-event (October 2023) 4 m resolution DEMs and differential models (DoD), providing a key data basis for high-resolution erosion quantification and mechanism analysis in this reach. To support the spatial analysis of erosion features, 272 cross-sections were generated at 250 m intervals along the channel centerline using ArcGIS and Python scripts. Pre-event DEM topographic profiles were automatically extracted for each cross-section. The cross-section numbers are labeled along the study reach in Fig. 1.

https://doi.org/10.5194/egusphere-2026-6278
Preprint. Discussion started: 16 November 2026
© Author(s) 2026. CC BY 4.0 License.

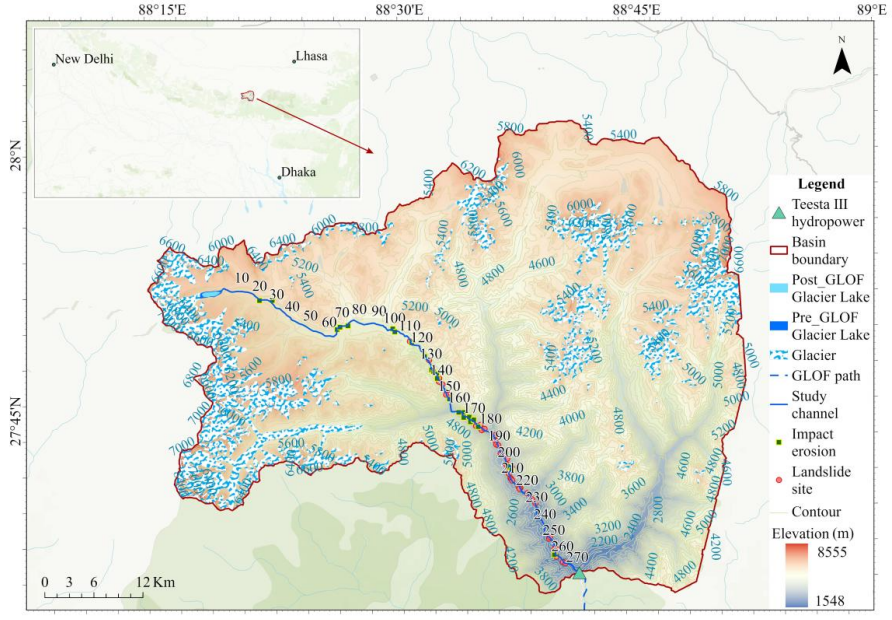


Figure 1. Location of the study area and geomorphic characteristics of the SLL basin. Left panel: regional location map showing Sikkim, Nepal, Bhutan, and the Tibet border, and the location of the Teesta-III hydropower station. Right panel: detailed topographic map showing glacier distribution, pre- and post-event lake extent, basin boundary, GLOF path, study reach, impact erosion sites (green squares), landslide sites (red circles), cross-section numbers, and elevation and contour information (elevation range 1548–8555 m). Basemap source: World Topographic Map (Sources: Esri, DeLorme, HERE, TomTom, Intermap, increment P Corp., GEBCO, USGS, FAO, NPS, NRCAN, GeoBase, IGN, Kadaster NL, Ordnance Survey, Esri Japan, METI, Esri China (Hong Kong), swisstopo, MapmyIndia, and the GIS User Community | Powered by Esri).

2.2 Data Sources and Preprocessing

The core datasets include pre- and post-event high-resolution digital elevation models (DEMs) and differential DEMs (DoD). The pre-event DEM was acquired in December 2018 at 4 m spatial resolution with vertical accuracy of about 1 m, derived from commercial satellite stereo pairs; the post-event DEM was acquired in October 2023 at 4 m resolution with vertical accuracy of about 0.8 m, generated from WorldView-3 stereo pairs. DoD was obtained by subtracting the pre-event DEM from the post-event DEM, resampled to a 4 m grid; negative values indicate erosion, positive values indicate deposition.

For remote sensing imagery, pre-event imagery used World Imagery Wayback 7 February 2023 images (0.6 m resolution); post-event imagery used World Imagery Wayback 8 January 2024 images (0.6 m resolution, partial coverage), supplemented by Google Earth historical imagery (Imagery © 2026 Airbus, Map data © 2026 Google). Landslide inventory was from 39 landslide polygons in the supplementary materials of Sattar et al. (2025). The peak water surface profile was obtained from HEC-

https://doi.org/10.5194/egusphere-2026-6278
Preprint. Discussion started: 16 November 2026
© Author(s) 2026. CC BY 4.0 License.

RAS 2D hydrodynamic simulation with Manning's n of 0.05 to match Sattar et al. (2025); the simulated GLOF arrival time at the Teesta Stage-III dam 68 km downstream was 2 h 13 min, close to the 2 h 22 min reported by Sattar et al. (2025); the computed maximum velocity and mud depth at that location were 9.4 m/s and 11.3 m, close to the reported 9.0 m/s and 9.0 m, supporting the validity of the simulation. All spatial data were projected to WGS 1984 UTM Zone 45N. The simulated maximum flow depths and maximum flow velocities along the study reach are shown in Fig. 2. Flow depth generally increases downstream as the valley narrows and the flow becomes confined, reaching 40.33 m in the deepest section, while the highest velocities of up to 31.55 m/s occur in the steep, confined reaches and at sharp bends, consistent with the spatial pattern of enhanced erosion.

The GLOF hydrograph was based on HEC-RAS 2D simulation results from Sattar et al. (2025) (Fig. 3). The hydrograph shows that discharge increased slowly in the initial stage, then sharply rose to a peak of about 48,500 m³/s, followed by rapid recession. Because bank erosion mainly occurs during high-flow periods, and following previous studies on dam-break floods and debris flow scour, we assumed that bank erosion occurred mainly during the period when discharge exceeded 1000 m³/s. This effective duration was 3700 s (pink arrow in Fig. 2). Bank retreat rate was calculated as $E = D_L / t$, where D_L is the local maximum horizontal retreat distance measured at the bend apex cross-section, perpendicular to the channel centerline, from the pre-event bank line to the post-event bank line. For shear scour segments, D_L was measured at representative cross-sections perpendicular to the channel centerline. The reported mean bank retreat rate is the average of E over all sites of each type. t =3700 s is the effective erosion duration during which discharge exceeded 1000 m³/s. This simplification avoids the uncertainty caused by including low-flow stages and ensures that the calculated erosion rates can be compared across different cross-sections.

Remote sensing imagery analysis supported the identification and classification of bank retreat features. Pre-event (7 February 2023) and post-event (8 January 2024) World Imagery Wayback scenes (https://livingatlas.arcgis.com/wayback/#mapCenter) at 0.6 m resolution were visually interpreted. Google Earth historical imagery supplemented coverage where needed. The pre-event imagery provided the baseline channel and bank configuration, including bank line positions, bar morphology, and vegetation cover. The post-event imagery revealed dramatic changes along the study reach, including extensive bank collapse scars, fresh steep bank faces, and newly deposited sediment fans at tributary junctions and along the main channel. Fig. 4 presents representative pre- and post-event imagery together with the corresponding bed elevation change for four key sites, and it also annotates bend impact sites (green squares) and identified landslide sites (red circles). Several sharp concave bends displayed deep, narrow erosion scars with steep, near-vertical walls and no obvious depositional fans at their bases. This morphology is distinct from the tongue-shaped deposits typically found below landslide scars, and these features were interpreted as the surface expression of bend-impact erosion. In contrast, landslide scars were identified by their arcuate head scarps and lobate deposits, and they were widely distributed along the steep valley slopes, particularly in the downstream narrow gorge. The imagery also showed that bend-impact scars were consistently located on the concave side of sharp bends, whereas shear scour features appeared as smoother, flow-parallel retreat surfaces on straight or gently curved sites. The bed-elevation-

https://doi.org/10.5194/egusphere-2026-6278
Preprint. Discussion started: 16 November 2026
© Author(s) 2026. CC BY 4.0 License.

change maps show that erosion (red) dominates the sharp bends and the confined reaches, while deposition (blue) concentrates in the wider sections and downstream of tributary junctions, further supporting the morphological criteria used in the classification workflow described in Section 3.1.

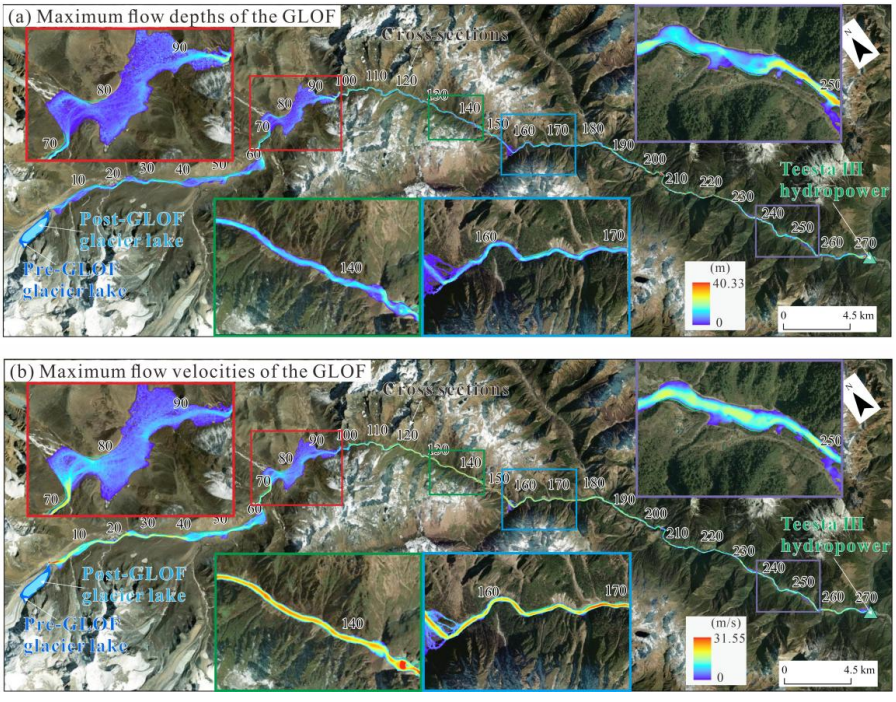


Figure 2. Simulated maximum flow depths (a) and maximum flow velocities (b) of the 2023 South Lhonak GLOF along the study reach. Cross-section numbers (10–270) are labeled along the reach. The post-event and pre-event glacier lake extents are marked. Insets show enlarged views of representative areas (red, green, blue, and purple boxes). Satellite/aerial basemap sources: World Imagery Wayback (Powered by Esri; Sources: Esri, Maxar, Earthstar Geographics, and the GIS User Community) and Google Earth historical imagery (Imagery © 2026 Airbus, Map data © 2026 Google).

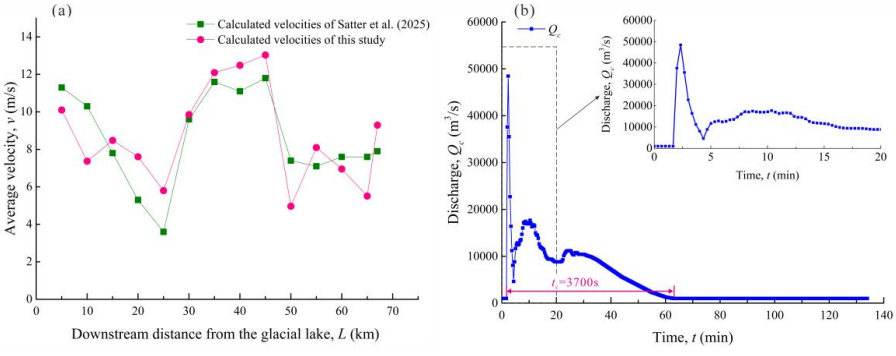


Figure 3. GLOF hydrograph and effective erosion duration. (a) Comparison between computed mean velocities and those of Sattar et al. (2025). The two datasets are consistent. (b) 2023 South Lhonak GLOF

https://doi.org/10.5194/egusphere-2026-6278
Preprint. Discussion started: 16 November 2026
© Author(s) 2026. CC BY 4.0 License.

hydrograph. The pink arrow marks the effective bank erosion period (t = 3700 s, discharge > 1000 m³/s). The inset shows the first 0–20 min, illustrating the abrupt rise to about 48,500 m³/s.

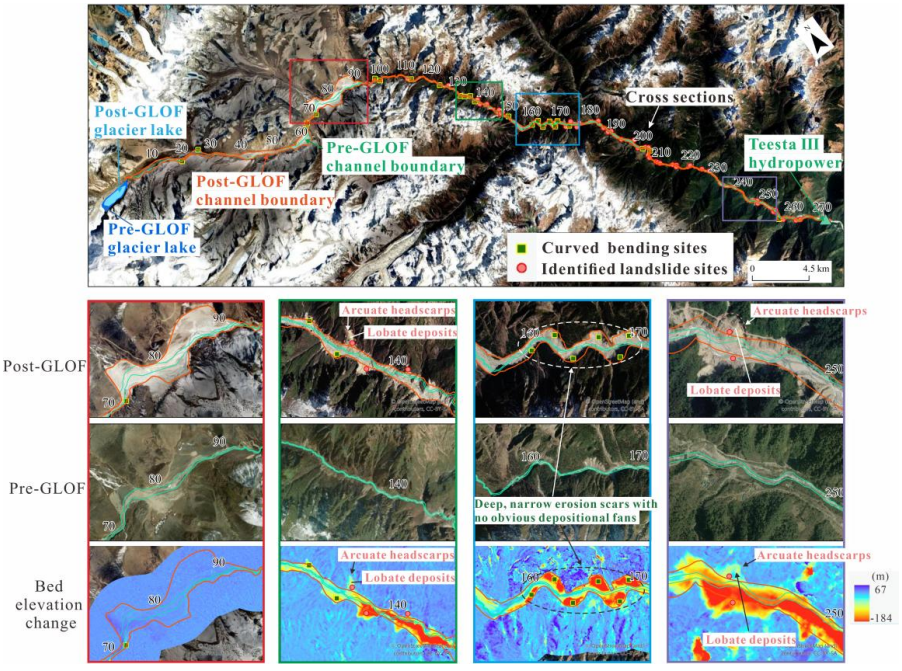


Figure 4. Remote sensing imagery and bed elevation change for four representative sites. Top row: post-event imagery with post-GLOF channel boundaries (orange) and pre-GLOF channel boundaries (cyan), bend impact sites (green squares) and identified landslide sites (red circles). Middle row: pre-event imagery with pre-GLOF channel boundaries. Bottom row: bed elevation changes from DoD, where negative values (red) indicate erosion and positive values (blue) indicate deposition. Annotations highlight arcuate head scarps, lobate deposits, and deep, narrow erosion scars with no obvious depositional fans. Pre- and post-event satellite/aerial imagery sources: World Imagery Wayback (Powered by Esri; Sources: Esri, Maxar, Earthstar Geographics, and the GIS User Community) and Google Earth historical imagery (Imagery © 2026 Airbus, Map data © 2026 Google).

3. Methods

3.1 Identification and separation of bank erosion mechanisms

This study concentrates on two distinct types of bank erosion, namely bend impact erosion and shear scour. Gravitational landslides were first identified and excluded based on diagnostic geomorphic features and an existing landslide inventory (Sattar et al., 2025). Landslide areas were identified by arcuate or chair-shaped head scarps. These were associated with tongue-shaped or fan-shaped deposits below (Fig. 4). These landslide sites were excluded from further bank erosion analysis. The remaining bank erosion polygons were classified into bend-impact erosion and shear scour. Bend-impact erosion was identified on the concave side of sharp bends. At these sites, the radius of curvature R_c is less than

https://doi.org/10.5194/egusphere-2026-6278
Preprint. Discussion started: 16 November 2026
© Author(s) 2026. CC BY 4.0 License.

20 times the channel width *B*. Diagnostic criteria included four conditions: (1) The site is on a concave bank with $R_c < 20B$; (2) The erosion long axis is approximately parallel to the concave bank line, which reflects lateral spreading of the impinging jet along the wall; (3) The DoD shows a narrow, deep incision with steep walls, signifying erosion depth is significantly greater than in surrounding areas; (4) There are no arcuate head scarps or associated deposits. Polygons satisfying all criteria were classified as bend-impact erosion. The remaining bank erosion polygons had smooth, channel-parallel boundaries and gentle retreat profiles. These were classified as shear scour. This classification scheme focuses on the two dominant types of bank erosion: bend impact erosion and shear scour. Gravitational landslides are explicitly excluded.

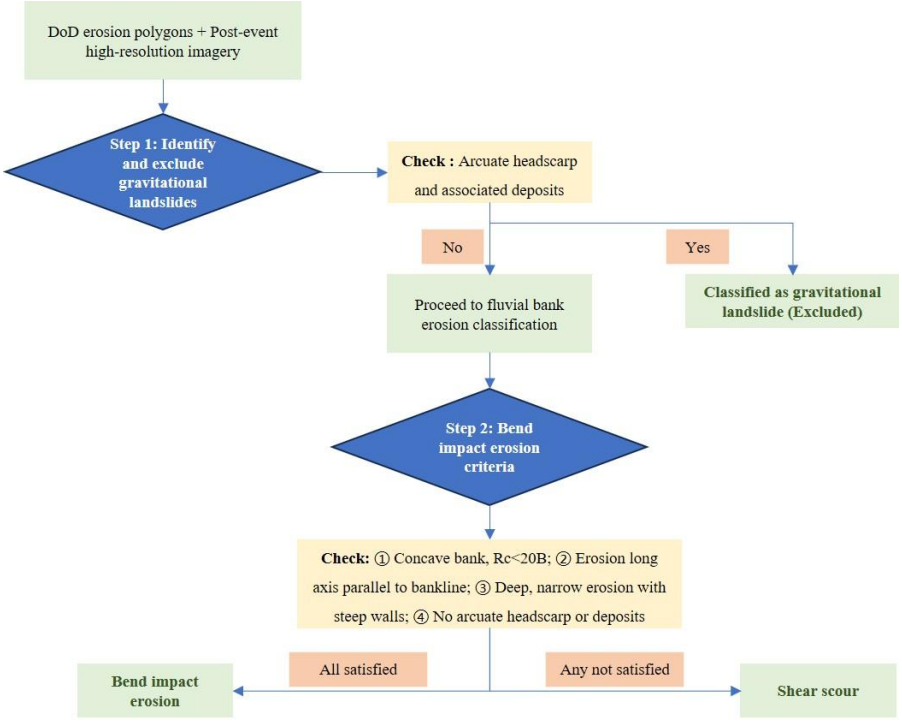


Figure 5. Decision tree for classifying bank retreat erosion polygons. Landslide areas are first identified and excluded based on diagnostic geomorphic features and an existing landslide inventory. Remaining bank erosion polygons are then classified as bend impact if they meet bend geometry and morphology criteria. Otherwise, they are shear scour.

3.2 Computation of the channel V-index

Valley cross-sectional form significantly influences GLOF propagation and associated bank erosion. To quantitatively characterize valley shape, this study adopted the V-index proposed by Zimmer and Gabet (2018). For a given cross-section, below a specified height H_s, the actual valley cross-sectional area A_x is compared with the area A_v of an ideal V-shaped profile of identical width and height:

https://doi.org/10.5194/egusphere-2026-6278
Preprint. Discussion started: 16 November 2026
© Author(s) 2026. CC BY 4.0 License.

$$V_{\text{index}} = (A_x - A_v) / A_v \quad (1)$$

where V_{index} is the normalized V-index (dimensionless), A_x is the actual valley cross-sectional area below a specified height H_s (m²), and A_v is the area of an ideal V-shaped profile with the same width and height (m²). A precisely V-shaped profile yields $V_{\text{index}} = 0$; wide valleys with actual area larger than the ideal V-shaped area yield $V_{\text{index}} > 0$; convex valley walls produce $V_{\text{index}} < 0$. Along the channel centerline, 272 cross-sections were generated at 250 m intervals from the pre-event DEM, and the V-index was computed for each cross section. Based on downstream changes in V_{index}, together with the longitudinal slope break at approximately 30 km, the study reach was divided into an upper segment (0–30 km), characterized by a wide valley and low gradient, and a lower segment (30–68 km), characterized by a narrower valley and steeper gradient. This provides a quantitative basis for analyzing the effects of channel morphology on erosion.

3.3 Mechanical model of bend impact erosion

The physical process of bend impact erosion can be summarized as follows: bend circulation concentrates flow energy toward the concave bank, and the flow then impacts the bank face as an oblique jet; erosion occurs when impact pressure exceeds material strength. This mode is hydraulically unique because inertia forces the flow to impact the concave bank at a near-normal angle when passing through sharp bends, constituting an oblique jet impinging on a solid boundary. In classical fluid mechanics, jet impact pressure is rigorously described by the momentum equation (Vennard, 1965), and it is widely applied in hydraulic energy dissipation and scour engineering. However, it has never been incorporated into quantitative GLOF bank erosion analysis, which has led to underestimation of bend erosion potential. Centrifugal force in bends creates a transverse water surface slope:

$$\Delta h = Bv^2 / gR_c \quad (2)$$

where Δh is the transverse water-surface elevation difference between the concave and convex banks (m), B is the channel width (m), v is the cross-sectional mean velocity (m s^{-1}), g is gravitational acceleration (m s^{-2}), and R_c is the radius of curvature (m). Based on the bend circulation theory (Mockmore, 1944), the near-bank velocity at the concave bank, $v_{concave}$ can reach about 1.2–1.5 times the cross-section mean velocity v (a value of 1.35 was adopted here)：

$$v_{concave} = \delta v \quad (3)$$

where $v_{concave}$ is the near-bank velocity at the concave bank (m s^{-1}) and δ is the velocity amplification coefficient (dimensionless; 1.35 adopted here). When flow impacts the concave bank face at incident angle θ, it can be idealized as an oblique planar jet impinging on a plate. From the momentum theorem, the total normal force exerted by the fluid on the wall is calculated by:

$$F = \rho_w A v_{concave}^2 \sin\theta \quad (4)$$

where F is the total normal impact force (N), ρ_w is water density (kg m^{-3}), A is the jet impingement area on the bank (m²), and θ is the incident angle between the flow direction and the bank

https://doi.org/10.5194/egusphere-2026-6278
Preprint. Discussion started: 16 November 2026
© Author(s) 2026. CC BY 4.0 License.

line (°). Accounting for energy losses and non-ideal effects, and using the normal kinetic energy $0.5C_c\rho_w v_{concave}^2 \sin^2\theta$ as the basis, the impact dynamic pressure is expressed as:

$$P_c = 0.5C_c\rho_w v_{concave}^2 \sin^2\theta \quad (5)$$

where P_c is the impact dynamic pressure (Pa) and C_c is the impact pressure coefficient (dimensionless; 1.5-1.8, set to 1.65 in this study). When impact pressure exceeds bank material strength S_t, erosion occurs, with erosion rate controlled by excess impact pressure:：

$$E_{impact} = K_{imp}(P_c - S_t) \quad (6)$$

where E_{impact} is the impact erosion rate (m s^{-1}), S_t is bank material strength (Pa), K_{imp} is the impact erodibility coefficient (m s^{-1} Pa^{-1}), calibrated from observed erosion data, and S_t is taken as 2c (c is cohesion, which is approximately 10–30 kPa for field moraine material).

To quantify the erosion signature of bend impact, the following metrics were extracted from DoD for each erosion polygon: (1) Effective erosion depth D_e, defined as the mean absolute value of negative DoD within the polygon (i.e., erosion volume divided by polygon area); and (2) Post-GLOF retreat wall slope angle α_{post}, obtained as the average slope of the erosion zone backwall from post-event DEM profiles. These parameters were compared between bend impact segments and straight shear segments.

3.4 Normalized bank erosion rate of shear scour segments

For shear scour segments, the normalized bank erosion rate was calculated following Zhao et al. (2022b):

$$r_l = \frac{E_l}{U_c} \cdot \frac{w_t}{w_c} \quad (7)$$

where r_l is the normalized bank erosion rate (dimensionless), E_l is the bank erosion rate (m s^{-1}), U_c is the near-bank flow velocity (m s^{-1}), w_t is the collapse block width (identified from post-event imagery), and w_c is the channel width (extracted from pre-event DEM).

To compute the normalized bank erosion rate, the ratio between bank height and flow depth (H_b / H_w, where H_b is bank height , and H_w is flow depth obtained from HEC-RAS simulation) is determined for each shear scour site. A high-elevation platform on the bank is identified as follows (Fig. 6). Based on the geomorphic principle that “platforms correspond to zones of significantly reduced slope,” for each cross-section we scanned horizontally from the valley bottom toward both banks. A point was considered to enter the platform zone when it satisfied both of the following conditions: (1) local slope computed from adjacent elevation differences and horizontal distances was below a threshold (slope Threshold is the local slope threshold, typically 5°–15°, set to 2° in this study); (2) the point elevation was higher than the valley bottom plus the average maximum flow depth on that side (H_w that is obtained from HEC-RAS simulation), ensuring the platform was not submerged during the flood. Once at least a minimum number of consecutive platform points (usually 3–5, set to 3 in this study) satisfied both conditions, the platform shoulder was marked. If a candidate platform contained fewer than two

https://doi.org/10.5194/egusphere-2026-6278
Preprint. Discussion started: 16 November 2026
© Author(s) 2026. CC BY 4.0 License.

points, it was considered invalid, and outputs were set to NaN. The platform extent was then extended outward until the slope steepened again or elevation fell below the constraint. Platform elevation was the mean elevation of the continuous low-slope zone, and bank height H_b was computed as the difference between platform elevation and valley bottom elevation. H_b / H_w was then calculated.

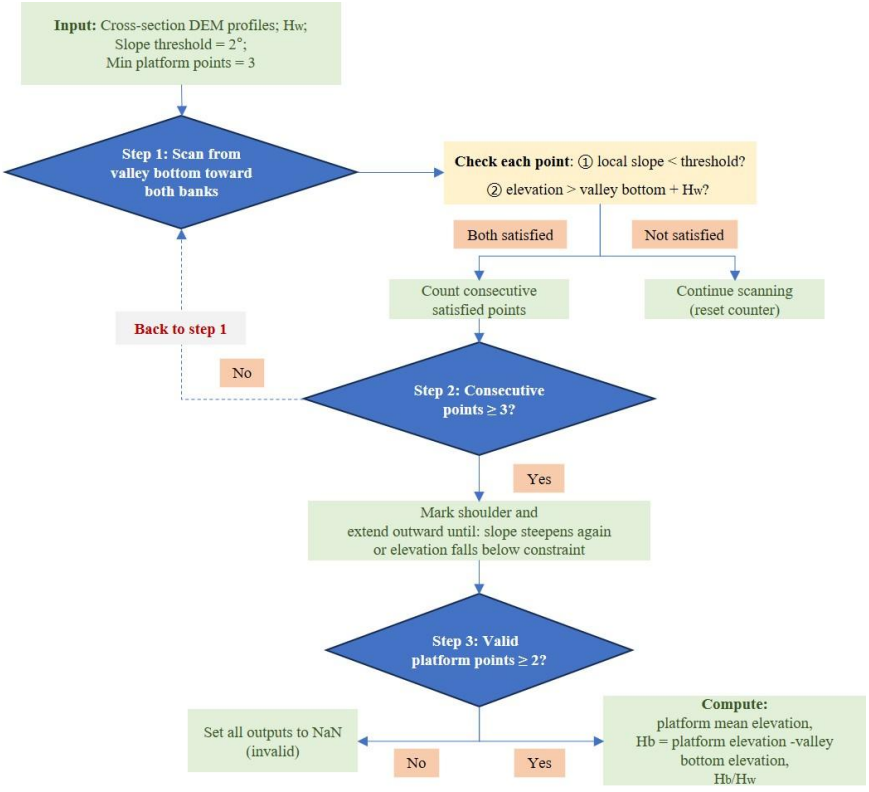


Figure 6. Flowchart for automatic identification of bank shoulders and calculation of H_b / H_w from cross-section DEM profiles. The algorithm scans laterally from the valley bottom. Points with local slope below 2° and elevation above the flood depth are defined as platform points; at least three consecutive points are required to mark a shoulder. Platform elevation yields bank height H_b, from which H_b / H_w is derived.

3.5 Calculation of apparent critical shear stress

In shear scour segments, the bank erosion rate was assumed to follow the excess shear stress equation:

$$E = k_d(\tau - \tau_c) \tag{8}$$

where the bank shear stress (empirical distribution for wide shallow channels) is obtained by $\tau = \rho_w g n^2 U_c^2 R_h^{-1/3}$, R_h is the hydraulic radius, numerically equal to H_w. The apparent critical shear stress was then obtained as:

https://doi.org/10.5194/egusphere-2026-6278
Preprint. Discussion started: 16 November 2026
© Author(s) 2026. CC BY 4.0 License.

$$\tau_c = \tau - E / k_d \quad (9)$$

k_d is the bank erodibility coefficient. Based on the Hanson and Simon (2001) erodibility classification for fine-grained soils, the changes in τ_c and their relationship with V_{index} were analyzed to investigate the effects of channel morphology on erosion thresholds.

4. Results

4.1 Valley morphology and spatial pattern of bank erosion

Figure 7 synthesizes the morphological characteristics and post-event responses of 272 cross-sections spanning the approximately 68-km-long study channel downstream of the breach. The four panels together reflect the macroscopic control of channel morphology on the spatial pattern of bank erosion.

Panel (a) presents the initial thalweg elevation, initial channel slope, and post-event bed elevation change along the reach. The longitudinal profile shows a clear break at approximately 30 km downstream of the breach, where the average slope increases from 3.2% in the upper segment to 7.0% in the lower segment. In the upper 30-km long segment, the initial elevation declines gently and the initial slope remains low, with only limited bed elevation adjustment. In the downstream 38-km long segment, the initial slope rises sharply while elevation drops rapidly, and the corresponding bed-change curve exhibits intense negative excursions indicative of strong bed incision, punctuated by localized positive excursions representing transient aggradation. This pattern reflects a highly nonlinear longitudinal adjustment concentrated in the lower segment, where the sudden increase in potential energy release generated a powerful incision impulse.

Panel (b) combines the V-index with a direct comparison of pre-event (red solid line) and channel width changes (red dotted line) to characterize the transverse evolution of valley morphology. In the upper 30-km segment, the V-index is consistently positive (mean 0.42, standard deviation 0.21, maximum 1.23), with a broad valley floor ranging from 300 to 600 m, typical of a glaciated U-shaped trough. Most of this segment shows negligible width change, but several locations (S59–S65, S74–S93) display large width changes. Inspection of the post-event imagery and DoD indicates that these changes are caused by debris-flow deposition rather than by bank erosion, and these locations were therefore excluded from the subsequent bank erosion rate calculation. Entering the lower 38-km segment, the V-index drops sharply toward zero and fluctuates between −0.2 and 0.8, with a mean of about 0.16, indicating a narrow and deeply incised valley with variable cross-sectional form. The channel width changes (red dotted line) are generally higher than those in the upper segment, indicating that bank erosion was intensified once the flow became tightly constrained.

https://doi.org/10.5194/egusphere-2026-6278
Preprint. Discussion started: 16 November 2026
© Author(s) 2026. CC BY 4.0 License.

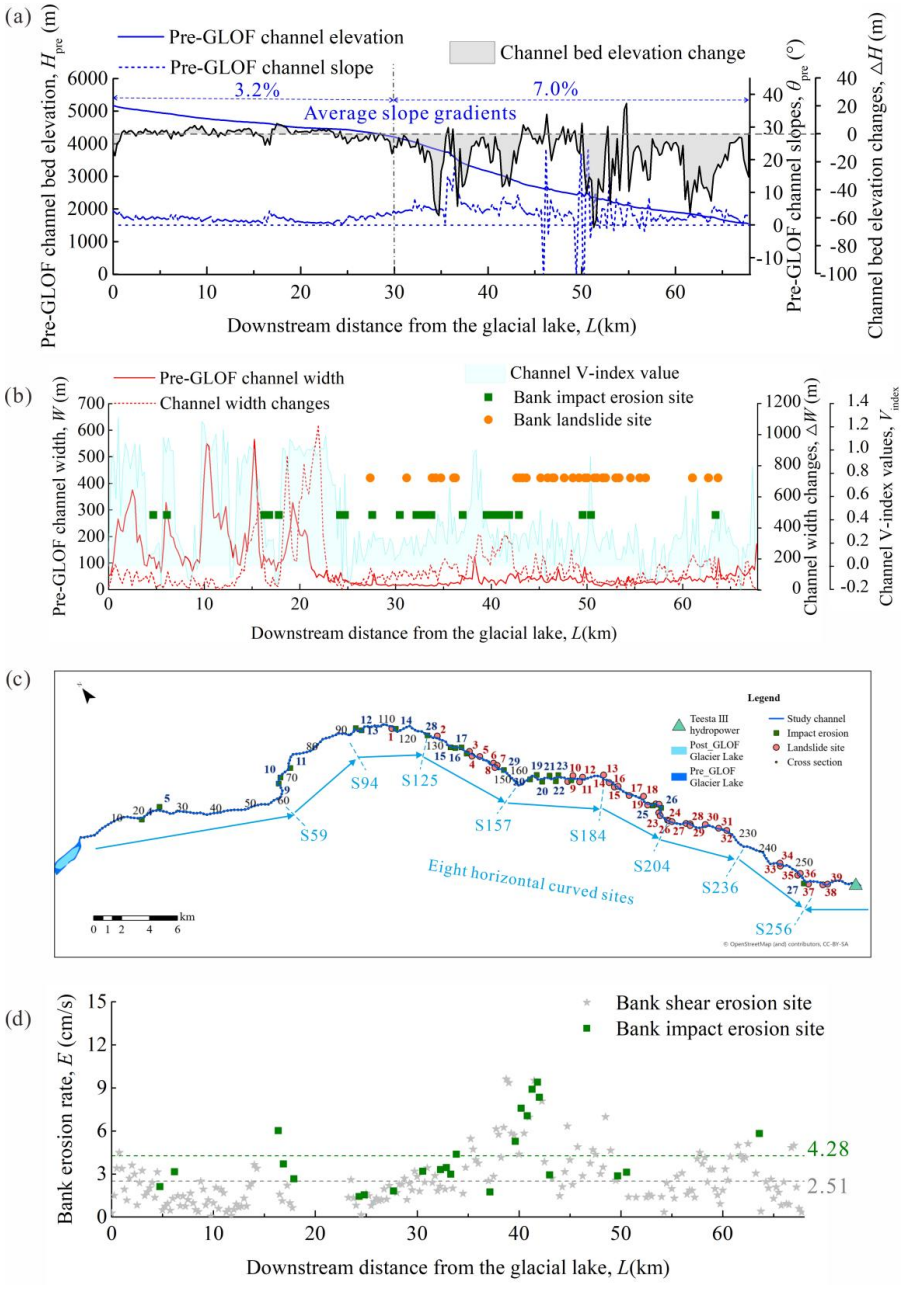


Figure 7. Initial and post-event valley morphology and spatial distribution of erosion. (a) Initial channel elevation, initial slope, and bed elevation change. Positive values indicate deposition. Negative values indicate erosion. (b) Pre-event channel widths, channel width changes, V-index, and spatial distribution of bend erosion sites (green squares) and landslide sites (orange circles). (c) Planform locations of lateral bends and corresponding cross-section numbers. (d) Bank erosion rates for shear scour and bend impact

https://doi.org/10.5194/egusphere-2026-6278
Preprint. Discussion started: 16 November 2026
© Author(s) 2026. CC BY 4.0 License.

sites, with mean values of 2.51 and 4.28 cm/s, respectively.

Panel (c) shows the planform distribution of bend impact erosion sites (green squares), landslide sites (red circles), and cross sections. Bend impact erosion sites are distributed across the study reach, whereas landslide sites are mostly between 25 and 65 km. Panel (d) shows that the mean local maximum bank retreat rate at bend apex cross-sections is 4.28 cm/s for bend impact sites and 2.51 cm/s for shear scour sites. The higher bank erosion rate at bend impact sites reflects their concentration at sharp concave bends, where flow impingement generates high normal pressures that more effectively remove bank material than the tangential shear stresses along straight or gently curved segments.

The combined scatter and planform information in Panels (b) and (c) reveals that bend-impact erosion sites are mostly clustered within the segment where the V-index is low, particularly at sharp bends such as S94, S125, S157, and S184. This spatial clustering is not coincidental: Panel (a) demonstrates that this segment experienced the most dramatic slope change and hence the highest flow energy, while Panel (b) shows that valley narrowing concentrated that energy within a confined channel, and the multiple bends visible in Panel (c) provided the geometric conditions necessary for high-energy flow to impinge directly on concave banks. Taken together, these observations establish a clear association between downstream channel steepening, bend geometry, and the occurrence of bend impact erosion.

The break in the longitudinal profile (approximately 30-km from the breach of the GLOF) separates two contrasting geomorphic regimes. The upper segment is characterized by a broad, low-gradient valley with negligible width change and limited bank erosion. The lower segment is characterized by a steeper gradient, narrower valley, and much higher bank erosion rates, especially concentrated bend impact erosion.

4.2 Morphological and mechanical characteristics of bend impact erosion

To clarify the differences between bend impact and shear scour, effective erosion depth D_e (erosion volume divided by polygon area) and bank slope angle α were extracted from the DoD and the pre- and post-event DEMs for bend impact sites and their adjacent shear sites (Fig. 8). The adjacent shear sites are those immediately upstream or downstream of each bend impact site, so that these two sites are spatially matched and the comparison is not confounded by the difference in erosion intensity.

The results reveal a striking contrast between the two types of bank erosion. In terms of effective erosion depth (Fig. 8a), bend impact segments display a mean D_e of approximately 52.7 m, with a range of 19.1–100.5 m, whereas adjacent shear segments have a mean D_e of only 15.2 m, ranging from 3.15 to 48.6 m. The former is thus nearly four times the latter. The comparison of bank slope angles further reinforces this geometric contrast. Pre-event slopes (Fig. 8b) show negligible differences between the two segment types. Post-event bank slope angles (Fig. 8c) in bend impact segments range from 48.5° to 77.6°, with a mean of approximately 61.8°, forming typical near-vertical cliff faces. In contrast, adjacent shear segments range from 8.8° to 57.2°, with a mean of about 40.7°, which is considerably gentler. When D_e and α are examined jointly (Fig. 9), the bend impact and adjacent shear populations are clearly separated, confirming that these two types of bank erosion are fundamentally

https://doi.org/10.5194/egusphere-2026-6278
Preprint. Discussion started: 16 November 2026
© Author(s) 2026. CC BY 4.0 License.

distinct in three-dimensional geometry.

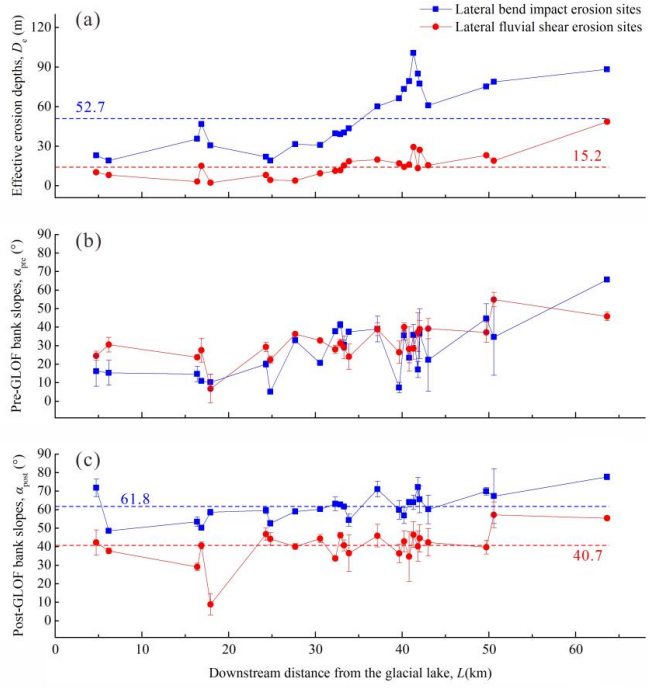


Figure 8. Comparison of effective erosion depth and bank slope between bend impact and adjacent shear segments. (a) Effective erosion depth D_e (bend segments show a high-value unimodal distribution, shear segments show a low-value broad distribution). (b) Pre-event bank slope angle α_{pre}. (c) Post-event bank slope angle α_{post}. The panels illustrate the deep and steep morphology of bend impact segments versus the shallow and gentle morphology of shear scour segments.

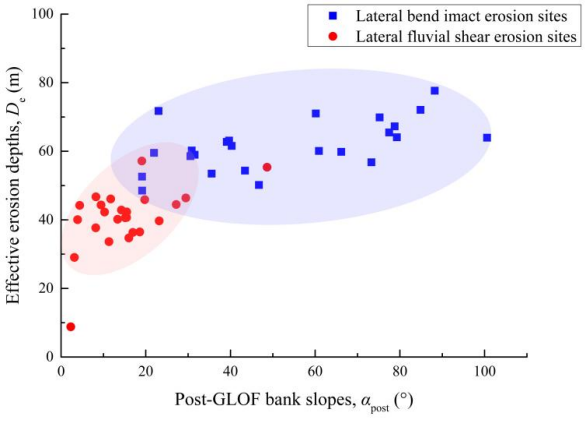


Figure 9. Joint distribution of effective erosion depth (D_e) and post-event bank slope (α_{post}) for bend impact (blue squares) and adjacent shear scour (red circles) sites. Shaded ellipses indicate the

https://doi.org/10.5194/egusphere-2026-6278
Preprint. Discussion started: 16 November 2026
© Author(s) 2026. CC BY 4.0 License.

concentration ranges of the two populations. The clear separation toward high D_e and high α_{post} for bend impact sites confirms the fundamentally different three-dimensional erosion geometry.

It is important to note that the bank erosion rates reported in Section 4.1 are averaged over all sites of each type across the full reach, whereas the effective erosion depths and bank slopes reported here are extracted at spatially matched sites: bend impact sites and their adjacent shear sites. The higher mean local maximum bank retreat rate of bend impact sites (4.28 cm/s, compared to 2.51 cm/s of shear scour sites) is accompanied by a much larger erosion depth. The volumetric erosion efficiency of bend impact, as reflected directly by D_e, is therefore several times greater than that of shear scour. This difference arises from the contrasting mechanics of the two types of bank erosion. In bend impact sites, flow is concentrated on the concave bank by centrifugal force, producing both a high normal impact pressure and intense toe scour. The loss of basal support triggers cantilever collapse of the upper bank and leads to the observed steepening. In relatively straight shear scour segments, by contrast, flow acts almost parallel to the bank line, and the bottom shear is generally insufficient to trigger large wedge failures. Slopes therefore remain near their angle of repose, with retreat occurring mainly by surface stripping.

Mechanical verification using the HEC-RAS 2D simulation results yields concave-bank velocities $v_{concave}$ of 6–20 m/s and incident angles θ of 26.8°–75.4° at the 24 identified bend impact sites. Applying the impact pressure formula (Eq. 5) with C_c = 1.65 gives impact pressures P_c ranging from 30.4 to 258.7 kPa, with a mean of about 128.8 kPa. For comparison, the estimated tensile/compressive strength S_t of the moraine and strongly weathered gneiss in the study area ranges from 20 to 60 kPa (assuming $S_t \approx$ 2c, with c = 10–30 kPa). All bend impact sites have P_c exceeding S_t by factors of 0.5–12.9, satisfying the impact erosion criterion. Bank shear stresses at these sites are only 0.08–1.01 kPa, yielding ratios of impact forces to shear stresses ranging from 162 to 585, with an average of approximately 284. This enormous disparity demonstrates that normal impact pressure is the overwhelmingly dominant force at sharp concave banks, while the contribution of bank-parallel shear stress is negligible.

4.3 Normalized bank erosion rate of shear scour segments

The ratio between bank height and flow depth (H_b / H_w) and the normalized bank erosion rate (r_l) were computed for all shear scour segments. The calculated data form a striking “horizontal funnel” configuration in the $r_l - H_b / H_w$ plane (Fig. 10). At the left end of the distribution, corresponding to low H_b / H_w values, the data points are stretched vertically over several orders of magnitude, whereas toward the right end, at high H_b / H_w values, the vertical scatter contracts progressively and the points converge into a comparatively narrow band.

In the low H_b / H_w range, the bank is relatively low while the flow depth is comparatively large, such that the water covers most of the bank face. Under these conditions, the bank erosion rate is governed primarily by local hydrodynamic forcing. The strong spatial variability in near-bank velocity,

https://doi.org/10.5194/egusphere-2026-6278
Preprint. Discussion started: 16 November 2026
© Author(s) 2026. CC BY 4.0 License.

shear stress, and bank material properties, exacerbated by local heterogeneities such as interbedded layers and scattered boulders, generates a very wide range of r_l values. In this regime, the erosion rate is effectively dictated by the local capacity of the flow: where the flow is strong, r_l is exceptionally high; where the flow approaches the critical shear stress, r_l is low or negligible. The large vertical spread at the left of the funnel therefore reflects the high sensitivity of bank erosion to spatial variations in hydrodynamic forcing.

In the high H_b / H_w range, in contrast, the bank is much higher relative to the flow depth, and the GLOF acts only on the toe while the upper bank remains in a cantilevered condition. Here, bank retreat is no longer directly controlled by the intensity of flow over the entire bank face; instead, it is paced by the cycle of toe undercutting, tension crack development, cantilever collapse, and sediment removal. Because the timescale of this cycle is determined primarily by bank geometry and material strength rather than by local flow intensity, the substantial hydrodynamic differences among cross-sections are effectively smoothed out, and the resulting r_l values are compressed into a relatively narrow range. The convergence of the data at high H_b / H_w thus marks a transition from hydrodynamic control to bank-stability control.

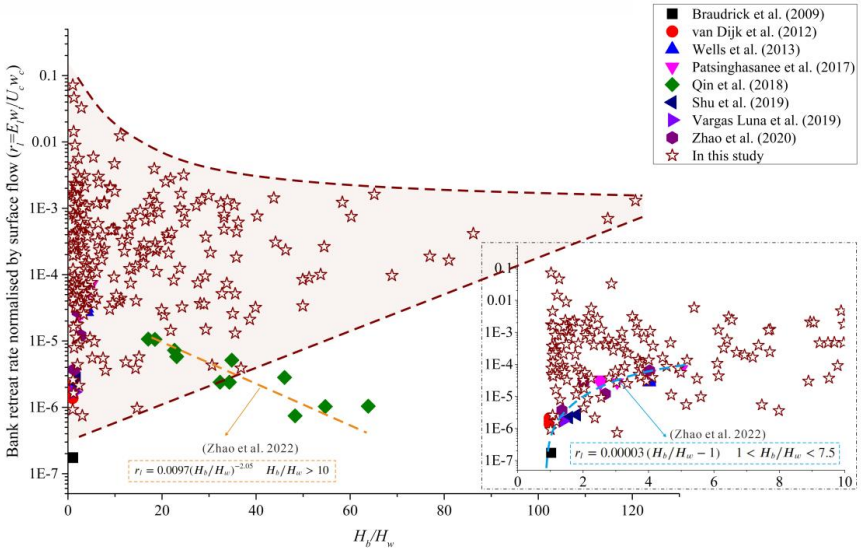


Figure 10. Normalized bank erosion rate of shear scour segments as a function of the ratio between bank height and flow depth. Previous experimental studies (Braudrick et al., 2009; van Dijk et al., 2012; Patsinghasanee et al., 2017; Qin et al., 2018; Shu et al., 2019; Vargas-Luna et al., 2019; Wells et al., 2013; Zhao et al., 2020), and the piecewise function of Zhao et al. (2022b) are shown for reference. Calculated data from DEM differencing and HEC-RAS simulation (stars) form a horizontal funnel, with wide scatter at low H_b / H_w and progressive narrowing at high H_b / H_w. The inset shows local

https://doi.org/10.5194/egusphere-2026-6278
Preprint. Discussion started: 16 November 2026
© Author(s) 2026. CC BY 4.0 License.

enlargement for $1 < H_b / H_w < 10$. The funnel indicates a shift from hydrodynamic dominance to bank-stability control.

The upper boundary of the funnel has a clear physical meaning: it represents the maximum erosion rate attainable at a given H_b / H_w. At the left of the diagram, this upper bound is set by the maximum hydrodynamic capacity and can be very high; toward the right, however, the upper bound declines because the cantilever cycle time increases with bank height, imposing a physical limit on the maximum retreat rate. The lower boundary represents the minimum erosion rate that can be detected, which is governed by the critical shear stress required to initiate erosion. At low H_b / H_w, this lower bound is low because even weak flow can initiate erosion, whereas at high H_b / H_w, the shallower flow reduces the applied shear stress toward the critical value, making erosion progressively harder to initiate and raising the lower bound. The convergence of the upper and lower boundaries at high H_b / H_w therefore provides a clear geometric expression of the shift from hydrodynamic to bank-stability control.

4.4 Apparent critical shear stress and erodibility of shear scour segments

Based on the excess shear stress equation $E = k_d(\tau - \tau_c)$, segmented linear inversion was performed for the shear scour segments to obtain the erodibility coefficient k_d and the apparent critical shear stress τ_c for each segment (Fig. 11). Most segments show reasonably good linear relationships between erosion rate and shear stress, with coefficients of determination (R^2) ranging from 0.50 to 0.85. The best fits occur in segments (b) and (e), with R^2 values of 0.787 and 0.848, respectively. Segment (a), by contrast, yields an R^2 of only 0.0009 and an inverted τ_c as high as 7399 Pa. This anomaly likely arises because the segment is located immediately downstream of the breach, where the flow is highly non-uniform and strongly turbulent, and a simple linear shear model is unable to capture the complexity of the erosion dynamics.

The inverted parameters display pronounced downstream heterogeneity. The apparent critical shear stress τ_c varies enormously, from a minimum of 5.67 Pa in segment (e) to a maximum of 130.57 Pa in segment (d). The erodibility coefficient k_d likewise spans about one order of magnitude, from 0.02 in segment (a) to 0.161 in segment (g). Such large variations reflect substantial differences in the resistance of bank materials under the extreme forcing of the flood. When the inverted τ_c and k_d values are plotted on the erodibility classification diagram of Hanson and Simon (Fig. 12) and compared with the landslide deposits of Chang et al. (2011) and the Jinwuco GLOF bank sediments of Li et al. (2025), a clear pattern emerges. All samples from this study fall within the “very erodible” category and are highly consistent with the data of Li et al. (2025). In contrast, the landslide deposits from the small-scale jet tests of Chang et al. (2011) plot mainly in the “resistant” to “moderately resistant” ranges. This difference suggests that the enormous flood power of natural-scale GLOFs can enhance the apparent erodibility of bank sediment, producing exceptionally high k_d values.

These results show that under extreme GLOF conditions, changes in channel morphology alter the

https://doi.org/10.5194/egusphere-2026-6278
Preprint. Discussion started: 16 November 2026
© Author(s) 2026. CC BY 4.0 License.

degree of flow energy concentration and significantly lower the apparent critical initiation threshold of bank material. This finding has important theoretical and practical implications for flood erosion modeling and risk assessment in complex mountain river basins. Moreover, the positions of the inverted k_d and τ_c values on the Hanson classification diagram provide a rapid means of identifying sites most susceptible to severe bank erosion, thereby supporting hazard early warning. For the upstream wide-valley segment (Fig. 11a), where the linear model fails, more complex nonlinear models or coupled hydrodynamic approaches will be needed in future research.

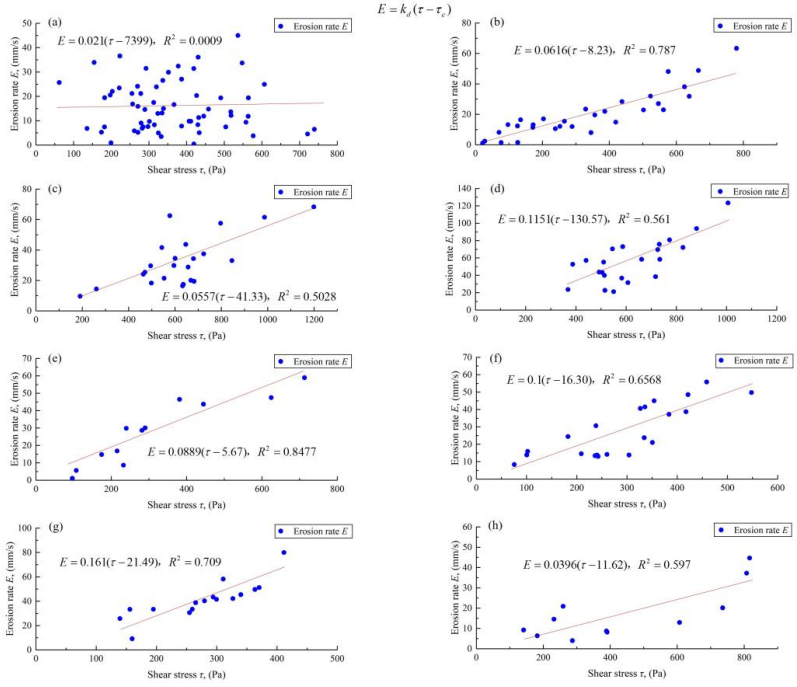


Figure 11. Segmented linear fits of erosion rate E versus shear stress τ based on the excess shear stress model. Segments: (a) S1–S93; (b) S94–S124; (c) S125–S156; (d) S157–S182; (e) S184–S203; (f) S204–S235; (g) S236–S255; (h) S256–S267. The slope represents the erodibility coefficient k_d, and the x-axis intercept represents the critical shear stress τ_c. The poor fit in (a) reflects the influence of strong turbulence of the GLOF immediately downstream of the breach.

https://doi.org/10.5194/egusphere-2026-6278
Preprint. Discussion started: 16 November 2026
© Author(s) 2026. CC BY 4.0 License.

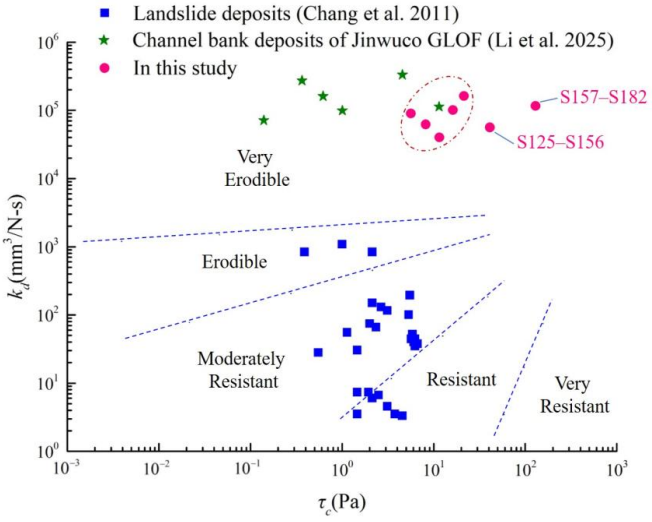


Figure 12. Comparison of soil erodibility classification. Inverted τ_c and k_d from this study (pink circles), GLOF bank sediments (green stars) of Li et al. (2025), and landslide deposits (blue squares) of Chang et al. (2011) plotted on the Hanson–Simon classification diagram. All samples from this study fall within the "very erodible" category.

5. Discussion

5.1 Methodological rationality of bank erosion identification and separation

The separation strategy adopted in this study—identifying and excluding gravitational landslides based on diagnostic geomorphic features and an existing inventory, and then classifying the remaining bank erosion into bend impact erosion and shear scour—rests on two key premises. First, landslide areas can be reliably identified from high-resolution post-event imagery by their diagnostic features, including arcuate or chair-shaped head scarps and associated tongue-shaped or fan-shaped deposits. Second, the mechanical magnitude difference between bend impact and shear scour spans roughly two orders of magnitude, with impact pressures of 30–259 kPa versus bank shear stresses of only 0.08–1.01 kPa. This large disparity makes the classification of "impact-dominated" at sharp concave banks mechanically robust rather than subjective. These two types of bank erosion also produce clearly different geomorphic signatures: bend impact erosion creates deep incisions and near-vertical cliff faces, whereas shear scour produces smooth and gentle retreat profiles. These signatures provide operational criteria for classification using imagery and DoD.

Nevertheless, this strategy has unavoidable uncertainties. When landslide deposits are completely transported by the GLOF, their geomorphic expression may lead to possible misclassification into shear or impact categories. In particular, small collapses triggered by impact may be indistinguishable from bend impact erosion if the sediment is instantly removed, causing an underestimation of the indirect gravitational contribution within the bend impact erosion sites. Moreover, at gentle bends with larger

https://doi.org/10.5194/egusphere-2026-6278
Preprint. Discussion started: 16 November 2026
© Author(s) 2026. CC BY 4.0 License.

curvature radii and smaller incident angles, the magnitude gap between impact and shear narrows, and the boundary of the classification may become blurred. These limitations imply that the separation strategy should be understood as a reasonable estimate of the dominant mechanism rather than an exact reconstruction of each retreat process. Future work with multi-temporal remote sensing or high-precision topographic data could further decompose the sequence of mechanisms in time and reduce classification uncertainty.

5.2 Classical theoretical basis and "depth-dominated" signature of bend impact erosion

The frontal impact of bend flow on concave banks has deep roots in classical fluid mechanics. Since Vennard (1965) systematically described the momentum analysis of jet impingement and Mockmore (1944) fully resolved the structure of bend circulation, bend flow has been understood as a complex superposition of the longitudinal main flow and transverse secondary circulation. At sharp bends, the centrifugal force generates a transverse water surface slope, raises the water level at the concave bank, and concentrates near-bank velocity. The main flow, driven by inertia, detaches from the convex bank and impinges directly on the concave bank, forming an equivalent oblique jet impact. This physical scene is widely used in hydraulic engineering for bridge pier scour, concave bank protection, and energy dissipation design, but it has been absent from GLOF geomorphology. By introducing the classical oblique jet impact theory into GLOF bank erosion analysis, this study establishes a complete quantitative chain from the momentum equation (Eq. 4) to impact dynamic pressure (Eq. 5) and then to erosion rate (Eq. 6). The average ratio between impact forces and shear stresses is approximately 284, demonstrating the absolute dominance of impact at sharp concave banks.

One of the most important findings of this study is the depth-dominated signature of bend impact erosion. Although bend impact sites also show a higher bank retreat rate than shear sites (4.28 vs. 2.51 cm/s), the difference in erosion depth is much more pronounced. The effective erosion depth D_e at bend impact sites is several times larger, and the bank slope angle α is closer to vertical. This characteristic can be explained by the mechanical nature of jet impingement. When a jet strikes a plate, the pressure is highest at the stagnation point, and the fluid subsequently spreads laterally along the wall. The impact pressure therefore decays rapidly along the wall direction but remains concentrated in the direction normal to the wall. Consequently, erosion develops in depth rather than laterally, forming narrow and deep incisions whose long axes are parallel to the bank line rather than to the main flow direction. This geometry is consistent with our observations in imagery and DoD (Fig. 4): the long axis of the deep incision is parallel to the bank line, not to the main flow. Because the detached debris is transported almost instantaneously by the high-velocity flow, no protective deposit accumulates at the slope toe, and the erosion face remains nearly vertical—a self-sharpening effect. In contrast, shear scour acts uniformly over the entire bank face, producing gentle slopes and shallow erosion. The combination of a higher retreat rate and a much greater erosion depth makes the volumetric erosion efficiency of bend impact far exceed that of shear scour. This finding implies that evaluating bank erosion intensity solely by retreat distance will seriously underestimate the hazard contribution of bend erosion. In GLOF erosion assessment, both erosion depth and volume must be considered.

https://doi.org/10.5194/egusphere-2026-6278
Preprint. Discussion started: 16 November 2026
© Author(s) 2026. CC BY 4.0 License.

5.3 Macroscopic control of channel morphology on bank erosion types

Combining the downstream variation of the V-index with the spatial distribution of erosion polygons reveals a clear macroscopic control chain: channel morphology determines the spatial allocation of flow energy, which in turn determines the dominant type of bank erosion and ultimately shapes the depth and morphology of bank retreat. In the upper 30-km segment, the valley floor is wide, and the flood spreads laterally across a cross-section hundreds of meters wide. The stream power per unit width is low, and the flow acts on the bank mainly through shear drag parallel to the bank. Bank erosion is limited, as indicated by the negligible width change, and is expressed as extensive floodplain scour and relatively gentle bank retreat. The erosion depth and slope fall within the lower to middle range of the overall statistics for shear scour segments.

In the lower 38-km segment, the valley narrows sharply, the cross-sectional area decreases rapidly, and the flow is forced to accelerate and concentrate, increasing the stream power per unit width. This segment contains multiple sharp bends with radius-to-width ratios less than 20, providing the necessary topographic conditions for bend impact. Although shear scour persists in straight or gently curved portions of the transitional segment, impact erosion replaces shear as the local dominant mechanism at sharp concave bends. The spatial statistics in Section 4.1 show that green squares representing bend impact erosion mostly cluster in this segment where V-index values are relatively low. At these locations, bend impact creates deep and steep faces (mean D_e 52.7 m, mean α_{post} 61.8°), far exceeding the typical values of straight shear segments (mean D_e 15.2 m, mean α_{post} 40.7°). Landslides are widely distributed in this segment (orange points in Fig. 7b), but their triggering is mainly related to intense incision and toe undercutting by flow in the narrow gorge, rather than to direct bend impact.

In summary, channel morphology controls bank erosion types at two levels. First, valley width determines the flow energy density and thus the overall erosion intensity. Second, channel curvature determines whether bend impact can occur and therefore controls the erosion mechanism type. In the lower segment where the valley is narrow and sharp bends coexist, both high energy density and sharp-bend geometry are present, allowing bend impact to emerge as an independent mechanism, form deep steep faces, and amplify landslide triggering. The predictive value of this control chain is that high-risk reaches can be identified before a GLOF occurs using only the pre-event DEM to compute V-index and channel curvature: narrow reaches with sharp bends are the most dangerous zones for bend impact and landslide initiation. At the same time, the depth-dominated signature of bend erosion revealed in this study indicates that hazard assessments focusing only on horizontal retreat distance will severely underestimate the erosion volume and associated sediment transfer and secondary hazard risks in bend reaches.

5.4 Limitations and outlook

The normalized bank erosion rate of shear scour segments forms a horizontal funnel in the r_l – H_b / H_w plane, with wide vertical scatter at low H_b / H_w and progressive narrowing at high H_b / H_w. This pattern reflects the shift in the dominant control on bank retreat as the ratio of bank height to flow

https://doi.org/10.5194/egusphere-2026-6278
Preprint. Discussion started: 16 November 2026
© Author(s) 2026. CC BY 4.0 License.

depth increases. This pattern has a clear physical interpretation. For hazard assessment, these patterns suggest that different reaches require different predictive approaches. Reaches with low H_b / H_w require detailed local flow simulation to capture the wide range of potential retreat, whereas reaches with high H_b / H_w can be assessed using bank stability criteria. The transition between these two regimes is gradual rather than sharply defined at a specific threshold.

There are several notable limitations in this study. The key parameters in the bend impact model—the impact pressure coefficient C_c, the impact erodibility coefficient K_{imp}, and the bank material strength S_t, are all rely on empirical assignment or indirect estimation and have not been calibrated by direct physical model experiments. The value of C_c = 1.65 is within the empirical range for high-Reynolds-number turbulent jets, but its applicability under the high-sediment, strongly unsteady conditions characteristic of GLOFs remains to be verified. Also, the extraction of effective erosion depth D_e and bank slope angle α is limited by the 4 m DoD resolution and the vertical accuracy of the DEMs (about 0.8–1 m). For areas where the erosion depth is smaller than the DEM error, the reliability of the calculated results decreases. Besides, this is a single-case study, and whether the funnel-shaped distribution of normalized bank erosion rate and the downstream variation of apparent critical shear stress are applicable to GLOFs of different scales and geological settings requires multi-case validation.

Future research can proceed in the following directions: (1) conduct scaled flume experiments on bend impact combined with coupled discrete element–smoothed particle hydrodynamics (DEM-SPH) numerical simulations to precisely calibrate the impact pressure coefficient and impact erodibility coefficient; (2) compile pre- and post-event high-resolution DEMs from more GLOF events worldwide to build a multi-case database and derive generalized parameterizations for the enhancement factor and apparent critical shear stress; (3) use multi-temporal remote sensing to track the temporal evolution of bank erosion and landslides during GLOFs, rather than inferring processes only from the final post-event landscape; and (4) integrate the bend impact model and bank erosion separation framework established in this study into two- or three-dimensional GLOF routing models to achieve dynamic coupled simulation of erosion and landslide triggering, providing a tool for full-hazard-chain prediction.

6. Conclusions

Based on a systematic analysis of the 2023 South Lhonak GLOF event, this study draws the following main conclusions:

(1) The longitudinal profile of the study channel shows a clear break at approximately 30 km downstream of the breach, where the average slope increases from 3.2% to 7.0% and the valley shifts from a broad, gentle form to a narrow, steep form. Most of the upper reach shows negligible width change and limited bank erosion, whereas the lower reach shows much larger width changes, with bend impact sites concentrated. The mean local maximum bank retreat rate at bend apex cross-sections is 4.28 cm/s for bend impact sites during the effective erosion period, higher than that of shear scour sites (2.51 cm/s).

(2) Bend impact is established as an independent type of bank erosion, based on classical jet impingement theory, and its depth-dominated signature is revealed. Impact pressures exceed bank shear

https://doi.org/10.5194/egusphere-2026-6278
Preprint. Discussion started: 16 November 2026
© Author(s) 2026. CC BY 4.0 License.

stresses by about two orders of magnitude. The effective erosion depth at bend impact sites (mean 52.7 m) is about four times that of adjacent shear scour sites (15.2 m), and the post-event bank slope at bend impact sites (mean 61.8°) is significantly steeper than that of adjacent shear scour sites (40.7°). The combination of a higher retreat rate and a much greater erosion depth indicates that evaluating bank erosion by retreat distance alone will seriously underestimate the volumetric contribution of bend impact erosion.

(3) The normalized bank erosion rate of shear scour segments exhibits a horizontal funnel distribution as a function of the ratio between bank height and flow depth (H_b / H_w), with wide scatter at low ratios and progressive narrowing at high ratios. This funnel pattern reflects a transition from hydrodynamic control, where local flow variability dominates, to bank-stability control, where cantilever collapse limits the retreat rate. GLOF-specific factors, including sediment abrasion, unsteady flow dynamics, and pre-existing fractures, further amplify the local variability of bank erodibility.

(4) The apparent critical shear stress was estimated from the excess shear stress model for each shear scour segment. Segmentally inverted τ_c and k_d vary widely (τ_c from 5.67 Pa to over 100 Pa, k_d spanning two orders of magnitude), and all samples fall within the "very erodible" category of the Hanson–Simon classification. These results indicate that extreme GLOF floods significantly enhance the apparent erodibility of bank soils, and that the apparent critical shear stress is strongly influenced by flow hydrodynamics and channel morphology.

(5) Channel morphology is the primary control on the spatial distribution and mechanisms of bank erosion in the study reach. The transition from a wide, low-gradient valley to a narrow, steep valley at approximately 30 km downstream of the breach coincides with a sharp increase in bank erosion intensity and a pronounced clustering of bend impact erosion, although bend impact also occurs upstream. This morphological control arises because valley width governs the concentration of flow energy, while channel curvature determines whether that energy is directed tangentially along the bank or normally onto the concave bank face. Consequently, pre-event channel morphology—specifically valley width and bend curvature—can be used to identify reaches most susceptible to deep bank erosion before a GLOF occurs, providing an operational basis for hazard zonation in GLOF-prone mountain valleys.

Data availability

The pre- and post-event DEMs used in this study were released by Sattar et al. (2025) and are available for download from https://doi.org/10.5281/zenodo.13122207. The landslide inventory was also obtained from the supplementary materials of Sattar et al. (2025). Satellite imagery was derived from World Imagery Wayback (https://livingatlas.arcgis.com/wayback) and Google Earth historical imagery (Imagery © 2026 Airbus, Map data © 2026 Google), which are publicly accessible. The HEC-RAS 2D simulation results, cross-section data, and all derived datasets generated in this study are available from the corresponding author upon reasonable request.

Authorship contributions

Conceptualization: P L, K H. Methodology: P L, L W. Writing (Original draft): P L. Methodology,

https://doi.org/10.5194/egusphere-2026-6278
Preprint. Discussion started: 16 November 2026
© Author(s) 2026. CC BY 4.0 License.

Validation: K H. Writing (review & editing): H L. Supervision: K H.

Declaration of interests

The contact author has declared that none of the authors has any competing interests.

Acknowledgements

We thank all members who contributed to the analysis of remote sensing imagery, including but not limited to Bozhang, Yifan Shu, and Jiangtao Chen.

Financial support

This work was financially supported by the National Key R&D Program of China (Grant No. 2025YFF0520003), the Sichuan Science and Technology Program (Grant No. 2026YFHZ0174), the Opening fund of State Key Laboratory of Geohazard Prevention and Geoenvironmental Protection (Grant No. SKLGP2026K006), and the Science and Technology Research Program of Key Laboratory of Mountain Hazards and Engineering Resilience, Chinese Academy of Sciences (Grant No. KLMHER-T12).

References

Aggarwal, S., Rai, S. C., Thakur, P. K., and Emmer, A.: Inventory and recently increasing GLOF susceptibility of glacial lakes in sikkim, eastern himalaya, Geomorphology, 295, 39–54, https://doi.org/10.1016/j.geomorph.2017.06.014, 2017.

Allen, S. K., Rastner, P., Arora, M., Huggel, C., and Stoffel, M.: Lake outburst and debris flow disaster at kedarnath, june 2013: hydrometeorological triggering and topographic predisposition, Landslides, 13, 1479–1491, https://doi.org/10.1007/s10346-015-0584-3, 2016.

Ballantyne, C. K., Sandeman, G. F., Stone, J. O., and Wilson, P.: Rock-slope failure following late pleistocene deglaciation on tectonically stable mountainous terrain, Quat. Sci. Rev., 86, 144–157, https://doi.org/10.1016/j.quascirev.2013.12.021, 2014.

Bolch, T., Kulkarni, A., Kääb, A., Huggel, C., Paul, F., Cogley, J. G., Frey, H., Kargel, J. S., Fujita, K., Scheel, M., Bajracharya, S., and Stoffel, M.: The state and fate of himalayan glaciers, Science, 336, 311–314, https://doi.org/10.1126/science.1215828, 2012.

Braudrick, C. A., Dietrich, W. E., Leverich, G. T., and Sklar, L. S.: Experimental evidence for the conditions necessary to sustain meandering in coarse-bedded rivers, Proceedings of the National Academy of Sciences, 106, 16936–16941, https://doi.org/10.1073/pnas.0909417106, 2009.

Chang, D. S., Zhang, L. M., Xu, Y., and Huang, R. Q.: Field testing of erodibility of two landslide dams triggered by the 12 May Wenchuan earthquake, Landslides, 8, 321–332, https://doi.org/10.1007/s10346-011-0256-x, 2011.

https://doi.org/10.5194/egusphere-2026-6278
Preprint. Discussion started: 16 November 2026
© Author(s) 2026. CC BY 4.0 License.



Cook, K. L., Andermann, C., Gimbert, F., Adhikari, B. R., and Hovius, N.: Glacial lake outburst floods as drivers of fluvial erosion in the himalaya, Science, 362, 53–57, https://doi.org/10.1126/science.aat4981, 2018.

Cui, P., Dang, C., Cheng, Z., and Scott, K. M.: Debris flows resulting from glacial-lake outburst floods in tibet, china, Phys. Geogr., 31, 508–527, https://doi.org/10.2747/0272-3646.31.6.508, 2010.

van Dijk, W. M., van de Lageweg, W. I., and Kleinhans, M. G.: Experimental meandering river with chute cutoffs, Journal of Geophysical Research: Earth Surface, 117, https://doi.org/10.1029/2011JF002314, 2012.

Dunning, S. A., Rosser, N. J., McColl, S. T., and Reznichenko, N. V.: Rapid sequestration of rock avalanche deposits within glaciers, Nat. Commun., 6, 7964, https://doi.org/10.1038/ncomms8964, 2015.

Furian, W., Maussion, F., and Schneider, C.: Projected 21st-Century Glacial Lake Evolution in High Mountain Asia, Front. Earth Sci., 10, https://doi.org/10.3389/feart.2022.821798, 2022.

Gouli, M. R., Hu, K., Khadka, N., Liu, S., Yifan, S., Adhikari, M., and Talchabhadel, R.: Quantitative assessment of the GLOF risk along china-nepal transboundary basins by integrating remote sensing, machine learning, and hydrodynamic model, Int. J. Disaster Risk Reduct., 118, 105231, https://doi.org/10.1016/j.ijdrr.2025.105231, 2025.

Govindha Raj, B. K., Kumar, V. K., and S.N., R.: Remote sensing-based inventory of glacial lakes in sikkim himalaya: semi-automated approach using satellite data, Geomatics Nat. Hazards Risk, 4, 241–253, https://doi.org/10.1080/19475705.2012.707153, 2013.

Hanson, G. J. and Simon, A.: Erodibility of cohesive streambeds in the loess area of the midwestern USA, Hydrological Processes, 15, 23–38, https://doi.org/10.1002/hyp.149, 2001.

Harrison, S., Kargel, J. S., Huggel, C., Reynolds, J., Shugar, D. H., Betts, R. A., Emmer, A., Glasser, N., Haritashya, U. K., Klimeš, J., Reinhardt, L., Schaub, Y., Wiltshire, A., Regmi, D., and Vilímek, V.: Climate change and the global pattern of moraine-dammed glacial lake outburst floods, Cryosphere, 12, 1195–1209, https://doi.org/10.5194/tc-12-1195-2018, 2018.

Intergovernmental Panel On Climate Change (Ipcc): Climate change 2021 – the physical science basis: working group I contribution to the sixth assessment report of the intergovernmental panel on climate change, Cambridge University Press, Cambridge, https://doi.org/10.1017/9781009157896, 2023.

Jiang, R., Lu, W., Xiao, S., He, X., Ju, L., Bai, R., Wei, M., and Zhang, L.: Erosion-deposition governs sediment dynamics and amplifies cascading hazards of glacial lake outburst floods, Geomorphology, 505, 110317, https://doi.org/10.1016/j.geomorph.2026.110317, 2026.

Kääb, A., Jacquemart, M., Gilbert, A., Leinss, S., Girod, L., Huggel, C., Falaschi, D., Ugalde, F., Petrakov, D., Chernomorets, S., Dokukin, M., Paul, F., Gascoin, S., Berthier, E., and Kargel, J. S.: Sudden large-volume detachments of low-angle mountain glaciers – more frequent than thought?, Cryosphere, 15, 1751–1785, https://doi.org/10.5194/tc-15-1751-2021, 2021.

Klimeš, J., Vilímek, V., and Benešová, M.: Landslide and glacial lake outburst flood hazard in the chucchún river basin, cordillera blanca, peru, AUC GEOGR., 50, 173–180,

https://doi.org/10.5194/egusphere-2026-6278
Preprint. Discussion started: 16 November 2026
© Author(s) 2026. CC BY 4.0 License.



https://doi.org/10.14712/23361980.2015.96, 2015.

Komori, J., Koike, T., Yamanokuchi, T., and Tshering, P.: Glacial lake outburst events in the Bhutan himalayas, Glob. Environ. Res., 16, 59–70, https://doi.org/10.57466/ger.16.1_59, 2012.

Li, S., Li, C., Li, P., Shu, Y., Li, Z., and Wang, Z.: Numerical investigation of the erosive dynamics of glacial lake outburst floods: a case study of the 2020 jinwuco event in southeastern Tibetan Plateau, Water, 17, 2837, https://doi.org/10.3390/w17192837, 2025.

Liu, W., Xiang, B., Jian, J., He, S., and Li, L.: A numerical study of the transition process from rock-ice avalanche to debris flow, Landslides, https://doi.org/10.1007/s10346-026-02701-4, 2026.

Mani, P., Allen, S., Evans, S. G., Kargel, J. S., Mergili, M., Petrakov, D., and Stoffel, M.: Geomorphic process chains in high-mountain regions—a review and classification approach for natural hazards assessment, Reviews of Geophysics, 61, e2022RG000791, https://doi.org/10.1029/2022RG000791, 2023.

McColl, S. T. and Davies, T. R. H.: Large ice-contact slope movements: glacial buttressing, deformation and erosion, Earth Surf. Processes Landforms, 38, 1102–1115, https://doi.org/10.1002/esp.3346, 2013.

Miles, E. S., Watson, C. S., Brun, F., Berthier, E., Esteves, M., Quincey, D. J., Miles, K. E., Hubbard, B., and Wagnon, P.: Glacial and geomorphic effects of a supraglacial lake drainage and outburst event, everest region, nepal himalaya, Cryosphere, 12, 3891–3905, https://doi.org/10.5194/tc-12-3891-2018, 2018.

Mockmore, C. A.: Flow around Bends in Stable Channels, Transactions of the American Society of Civil Engineers, 109, 593–618, https://doi.org/10.1061/TACEAT.0005737, 1944.

Nie, Y., Sheng, Y., Liu, Q., Liu, L., Liu, S., Zhang, Y., and Song, C.: A regional-scale assessment of himalayan glacial lake changes using satellite observations from 1990 to 2015, Remote Sens. Environ., 189, 1–13, https://doi.org/10.1016/j.rse.2016.11.008, 2017.

Patsinghasanee, S., Kimura, I., Shimizu, Y., Nabi, M., and Chub-Uppakarn, T.: Coupled studies of fluvial erosion and cantilever failure for cohesive riverbanks: Case studies in the experimental flumes and U-Tapao River, Journal of Hydro-environment Research, 16, 13–26, https://doi.org/10.1016/j.jher.2017.04.002, 2017.

Qin, C., Zheng, F., Wells, R. R., Xu, X., Wang, B., and Zhong, K.: A laboratory study of channel sidewall expansion in upland concentrated flows, Soil and Tillage Research, 178, 22–31, https://doi.org/10.1016/j.still.2017.12.008, 2018.

Sattar, A., Goswami, A., Kulkarni, Anil. V., Emmer, A., Haritashya, U. K., Allen, S., Frey, H., and Huggel, C.: Future glacial lake outburst flood (GLOF) hazard of the south lhonak lake, sikkim himalaya, Geomorphology, 388, 107783, https://doi.org/10.1016/j.geomorph.2021.107783, 2021.

Sattar, A., Haritashya, U. K., Kargel, J. S., and Karki, A.: Transition of a small himalayan glacier lake outburst flood to a giant transborder flood and debris flow, Sci. Rep., 12, 12421, https://doi.org/10.1038/s41598-022-16337-6, 2022.

Sattar, A., Cook, K. L., Rai, S. K., Berthier, E., Allen, S., Rinzin, S., de Vries, M. V. W., Haeberli, W., Kushwaha, P., Shugar, D. H., Emmer, A., Haritashya, U. K., Frey, H., Rao, P., Gurudin, K. S. K.,

https://doi.org/10.5194/egusphere-2026-6278
Preprint. Discussion started: 16 November 2026
© Author(s) 2026. CC BY 4.0 License.

Rai, P., Rajak, R., Hossain, F., Huggel, C., Mergili, M., Azam, Mohd. F., Gascoin, S., Carrivick, J. L., Bell, L. E., Ranjan, R. K., Rashid, I., Kulkarni, Anil. V., Petley, D., Schwanghart, W., Watson, C. S., Islam, N., Gupta, M. D., Lane, S. N., and Bhat, S. Y.: The Sikkim flood of October 2023: Drivers, causes, and impacts of a multihazard cascade, Science, 387, eads2659, https://doi.org/10.1126/science.ads2659, 2025.

Shrestha, F., Steiner, J. F., Shrestha, R., Dhungel, Y., Joshi, S. P., Inglis, S., Ashraf, A., Wali, S., Walizada, K. M., and Zhang, T.: A comprehensive and version-controlled database of glacial lake outburst floods in high mountain asia, Earth Syst. Sci. Data, 15, 3941–3961, https://doi.org/10.5194/essd-15-3941-2023, 2023.

Shu, A., Duan, G., Rubinato, M., Tian, L., Wang, M., and Wang, S.: An Experimental Study on Mechanisms for Sediment Transformation Due to Riverbank Collapse, Water, 11, 529, https://doi.org/10.3390/w11030529, 2019.

Shugar, D. H., Burr, A., Haritashya, U. K., Kargel, J. S., Watson, C. S., Kennedy, M. C., Bevington, A. R., Betts, R. A., Harrison, S., and Strattman, K.: Rapid worldwide growth of glacial lakes since 1990, Nat. Clim. Change, 10, 939–945, https://doi.org/10.1038/s41558-020-0855-4, 2020.

Shugar, D. H., Jacquemart, M., Shean, D., Bhushan, S., Upadhyay, K., Sattar, A., Schwanghart, W., McBride, S., de Vries, M. V. W., Mergili, M., Emmer, A., Deschamps-Berger, C., McDonnell, M., Bhambri, R., Allen, S., Berthier, E., Carrivick, J. L., Clague, J. J., Dokukin, M., Dunning, S. A., Frey, H., Gascoin, S., Haritashya, U. K., Huggel, C., Kääb, A., Kargel, J. S., Kavanaugh, J. L., Lacroix, P., Petley, D., Rupper, S., Azam, M. F., Cook, S. J., Dimri, A. P., Eriksson, M., Farinotti, D., Fiddes, J., Gnyawali, K. R., Harrison, S., Jha, M., Koppes, M., Kumar, A., Leinss, S., Majeed, U., Mal, S., Muhuri, A., Noetzli, J., Paul, F., Rashid, I., Sain, K., Steiner, J., Ugalde, F., Watson, C. S., and Westoby, M. J.: A massive rock and ice avalanche caused the 2021 disaster at chamoli, indian himalaya, Science, 373, 300–306, https://doi.org/10.1126/science.abh4455, 2021.

Singh, A., Anand, V., Durga Rao, K. H. V., P., S. R., and Chauhan, P.: Unveiling the catastrophic landslide-induced flash flood in teesta river, sikkim: insight from south lhonak glacial lake, Landslides, 22, 837–855, https://doi.org/10.1007/s10346-024-02378-7, 2025.

Taylor, C., Robinson, T. R., Dunning, S., Rachel Carr, J., and Westoby, M.: Glacial lake outburst floods threaten millions globally, Nat. Commun., 14, 487, https://doi.org/10.1038/s41467-023-36033-x, 2023.

Vargas-Luna, A., Duró, G., Crosato, A., and Uijttewaal, W.: Morphological Adaptation of River Channels to Vegetation Establishment: A Laboratory Study, Journal of Geophysical Research: Earth Surface, 124, 1981–1995, https://doi.org/10.1029/2018JF004878, 2019.

Vennard, J. K.: Elementary fluid mechanics, 4nd. ed., John Wiley, New York, 570 pp., 1965.

Wang, H., Cui, P., Li, Y., Tang, J., Wei, R., Yang, A., Zhou, L., Bazai, N. A., and Zhang, G.: Rock and ice avalanche-generated catastrophic debris flow at chamoli, 7 february 2021: new insights from the geomorphic perspective, Geomorphology, 452, 109110, https://doi.org/10.1016/j.geomorph.2024.109110, 2024.

Wang, X., Guo, X., Yang, C., Liu, Q., Wei, J., Zhang, Y., Liu, S., Zhang, Y., Jiang, Z., and Tang, Z.:

https://doi.org/10.5194/egusphere-2026-6278
Preprint. Discussion started: 16 November 2026
© Author(s) 2026. CC BY 4.0 License.

Glacial lake inventory of high-mountain asia in 1990 and 2018 derived from landsat images, Earth Syst. Sci. Data, 12, 2169–2182, https://doi.org/10.5194/essd-12-2169-2020, 2020.

Wells, R. R., Momm, H. G., Rigby, J. R., Bennett, S. J., Bingner, R. L., and Dabney, S. M.: An empirical investigation of gully widening rates in upland concentrated flows, CATENA, 101, 114–121, https://doi.org/10.1016/j.catena.2012.10.004, 2013.

Westoby, M. J., Dunning, S. A., Carrivick, J. L., Coulthard, T. J., Sain, K., Kumar, A., Berthier, E., Haritashya, U. K., Shean, D. E., Azam, Mohd. F., Upadhyay, K., Koppes, M., McCourt, H. R., and Shugar, D. H.: Rapid fluvial remobilization of sediments deposited by the 2021 Chamoli disaster, Indian Himalaya, Geology, 51, 924–928, https://doi.org/10.1130/G51225.1, 2023.

Yao, T., Xue, Y., Chen, D., Chen, F., Thompson, L., Cui, P., Koike, T., Lau, W. K.-M., Lettenmaier, D., Mosbrugger, V., Zhang, R., Xu, B., Dozier, J., Gillespie, T., Gu, Y., Kang, S., Piao, S., Sugimoto, S., Ueno, K., Wang, L., Wang, W., Zhang, F., Sheng, Y., Guo, W., Ailikun, Yang, X., Ma, Y., Shen, S. S. P., Su, Z., Chen, F., Liang, S., Liu, Y., Singh, V. P., Yang, K., Yang, D., Zhao, X., Qian, Y., Zhang, Y., and Li, Q.: Recent Third Pole's Rapid Warming Accompanies Cryospheric Melt and Water Cycle Intensification and Interactions between Monsoon and Environment: Multidisciplinary Approach with Observations, Modeling, and Analysis, Bull. Am. Meteorol. Soc., 100, 423–444, https://doi.org/10.1175/BAMS-D-17-0057.1, 2019.

You, Q., Cai, Z., Pepin, N., Chen, D., Ahrens, B., Jiang, Z., Wu, F., Kang, S., Zhang, R., Wu, T., Wang, P., Li, M., Zuo, Z., Gao, Y., Zhai, P., and Zhang, Y.: Warming amplification over the arctic pole and third pole: trends, mechanisms and consequences, Earth Sci. Rev., 217, 103625, https://doi.org/10.1016/j.earscirev.2021.103625, 2021.

Zhang, C., Qin, D.-H., and Zhai, P.-M.: Amplification of warming on the Tibetan Plateau, Adv. Clim. Change Res., 14, 493–501, https://doi.org/10.1016/j.accre.2023.07.004, 2023.

Zhang, Q., Hu, K., Liu, S., Wei, L., and Zhang, X.: Remote sensing interpretation of causes and dynamics of the gyirong outburst flood disaster, tibet, on July 8, 2025, Nat. Hazard., 122, 316, https://doi.org/10.1007/s11069-026-08081-1, 2026.

Zhang, T., Wang, W., and An, B.: A massive lateral moraine collapse triggered the 2023 south lhonak lake outburst flood, sikkim himalayas, Landslides, 22, 299–311, https://doi.org/10.1007/s10346-024-02358-x, 2025.

Zhao, F., Long, D., Li, X., Huang, Q., and Han, P.: Rapid glacier mass loss in the Southeastern Tibetan Plateau since the year 2000 from satellite observations, Remote Sens. Environ., 270, 112853, https://doi.org/10.1016/j.rse.2021.112853, 2022a.

Zhao, K., Gong, Z., Zhang, K., Wang, K., Jin, C., Zhou, Z., Xu, F., and Coco, G.: Laboratory Experiments of Bank Collapse: The Role of Bank Height and Near-Bank Water Depth, Journal of Geophysical Research: Earth Surface, 125, e2019JF005281, https://doi.org/10.1029/2019JF005281, 2020.

Zhao, K., Coco, G., Gong, Z., Darby, S. E., Lanzoni, S., Xu, F., Zhang, K., and Townend, I.: A review on bank retreat: mechanisms, observations, and modeling, Reviews of Geophysics, 60, e2021RG000761, https://doi.org/10.1029/2021RG000761, 2022b.

https://doi.org/10.5194/egusphere-2026-6278
Preprint. Discussion started: 16 November 2026
© Author(s) 2026. CC BY 4.0 License.



902 Zheng, G., Allen, S. K., Bao, A., Ballesteros-Cánovas, J. A., Huss, M., Zhang, G., Li, J., Yuan, Y.,
903 Jiang, L., Yu, T., Chen, W., and Stoffel, M.: Increasing risk of glacial lake outburst floods from
904 future Third Pole deglaciation, Nat. Clim. Chang., 11, 411–417, https://doi.org/10.1038/s41558-
905 021-01028-3, 2021.
906 Zimmer, P. D. and Gabet, E. J.: Assessing glacial modification of bedrock valleys using a novel
907 approach, Geomorphology, 318, 336–347, https://doi.org/10.1016/j.geomorph.2018.06.021, 2018.
908